Steady-state free precession with hyperpolarized ^{3}He: Experiments and theory

Jim M. Wild [a,*], Kevin Teh [a], Neil Woodhouse [a], Martyn N.J. Paley [a], Stan Fichele [a], Nicola de Zanche [b], Larry Kasuboski [c]

[a] *Unit of Academic Radiology, University of Sheffield, 'C' floor, Royal Hallamshire Hospital, Glossop Road, S10 2JF, UK*
[b] *Institute for Biomedical Engineering, University and ETH, Zurich, Switzerland*
[c] *Philips Medical Systems, Cleveland, OH, USA*

Abstract

The magnetization response of hyperpolarized ^{3}He gas to a steady-state free precession (SSFP) sequence was simulated using matrix product operators. The simulations included the effects of flip angle (α), sequence timings, resonant frequency, gas diffusion coefficient, imaging gradients, T_1 and T_2. Experiments performed at 1.5 T, on gas phantoms and with healthy human subjects, confirm the predicted theory, and indicate increased SNR with SSFP through use of higher flip angles when compared to optimized spoiled gradient echo (SPGR). Simulations and experiments show some compromise to the SNR and some point spread function broadening at high α due to the incomplete refocusing of transverse magnetization, caused by diffusion dephasing from the readout gradient. Mixing of gas polarization levels by diffusion between slices is also identified as a source of signal loss in SSFP at higher α through incomplete refocusing. Nevertheless, in the sample experiments, a SSFP sequence with an optimized flip angle of $\alpha = 20°$, and 128 sequential phase encoding views, showed a higher SNR when compared to SPGR ($\alpha = 8°$) with the same bandwidth. Some of the gas sample experiments demonstrated a transient signal response that deviates from theory in the initial phase. This was identified as being caused by radiation damping interactions between the large initial transverse magnetization and the high quality factor ($Q = 250$) birdcage resonator. In ^{3}He NMR experiments, performed without imaging gradients, diffusion dephasing can be mitigated, and the effective T_2 is relatively long ($\geqslant 1$ s). Under these circumstances the SSFP sequence behaves like a CPMG sequence with $\sin(\alpha/2)$ weighting of SNR. Experiments and simulations were also performed to characterize the off-resonance behaviour of the SSFP HP ^{3}He signal. Characteristic banding artifacts due to off-resonance harmonic beating were observed in some of the *in vivo* SSFP images, for instance in axial slices close to the diaphragm where B_0 inhomogeneity is highest. Despite these artifacts, a higher SNR was observed with SSFP *in vivo* when compared to the SPGR sequence. The trends predicted by theory of increasing SSFP SNR with increasing flip angle were observed in the range $\alpha = 10–20°$ without compromise to image quality through blurring caused by excessive k-space filtering.
© 2006 Elsevier Inc. All rights reserved.

Keywords: Steady-state free precession; ^{3}Helium; Hyperpolarized; Lungs; Diffusion

1. Introduction

The inert gas nuclei of ^{3}He and ^{129}Xe can be polarized to extremely high levels through the use of alternative polarization methods, such as spin exchange optical pumping [1].

This *hyperpolarization* enables applications of gas phase NMR that would have been impossible with the SNR constraints of Boltzmann polarization. One application is *in vivo* MRI, where hyperpolarized (HP) gas can provide high spatial and temporal resolution images of gas ventilation in the lungs and airways as well as physiologically useful functional information [2]. High spatial resolution imaging of gas ventilation with high SNR, requires efficient utilization of the finite hyperpolarization within the time course

of a human breath-hold. Most studies of human ventilation to date have used HP ^{3}He, and have imaged the lungs using 2D [2–5] or 3D [6], low flip-angle, spoiled gradient echo (SPGR) sequences. A low flip angle SPGR sequence provides a steady depletion of the finite polarization during the sampling of k-space, and therefore imparts less broadening of the point spread function (PSF) through k-space filtering, than high flip angles [7,8]. SPGR sequences can be further optimized to reduce blurring by provision of a steady magnetization response through use of a variable flip angle [7]. Refocused magnetization pulse sequences, such as steady-state free precession (SSFP) [9,10] and single shot multiple spin echo [11], have potential for increased SNR and spatial resolution for imaging with hyperpolarized (HP) agents by recycling residual transverse magnetization with the finite longitudinal magnetization. Previous work with SSFP using intravenous infusions of HP ^{13}C molecules (with long T_1 and T_2) [12] shows promising results for high SNR MR angiography. Recent preliminary work with HP ^{3}He in human lungs at 1.5 T [13,14], demonstrated higher SNR with SSFP when compared to SPGR low flip angle methods, although banding artifacts due to off-resonance effects were identified in regions of the lung of high B_0 inhomogeneity.

In the work presented here, the magnetization response of HP ^{3}He gas to a SSFP sequence was studied in detail with numerical simulations using product operator matrix methods. Experiments were then performed with SSFP on gas samples in phantoms and in human subjects to corroborate the simulations and these results were compared to results from SPGR methods, which are currently used as standard for ^{3}He ventilation imaging.

2. Methods

2.1. Simulations

A SSFP sequence, $\alpha/2 - TR/2 - (\alpha - TR)^n$, was modeled based on the pulse sequence structure depicted in Fig. 1. The phase of the α pulse (rotation about the x-axis) was alternated by π on alternate phase encode views, $n = 1, \ldots, N_y$. The evolution of the magnetization vector was simulated with product operator matrix methods, used previously for analysis of ^{1}H SSFP signal dynamics [15,16,18,19]. The theory was adapted for HP ^{3}He gas magnetic resonance to account for a non-renewable polarization and a contribution to the transverse signal decay from diffusion attenuation. The 3D magnetization vector immediately after the $(n + 1)$th RF pulse is given by:

$$\mathbf{M}^+(n + 1) = \mathbf{A}\mathbf{M}^+(n), \tag{1}$$

where

$$\mathbf{A} = \mathbf{PCR}_\pi(n)\mathbf{R}_\alpha\mathbf{PC}. \tag{2}$$

$\mathbf{P}$ represents the free precession matrix rotation during a period τ for a spin with a frequency-offset Δf_0. $\mathbf{C}$ is the relaxation matrix, $\mathbf{R}_\alpha$ is the rotation matrix of the α pulse
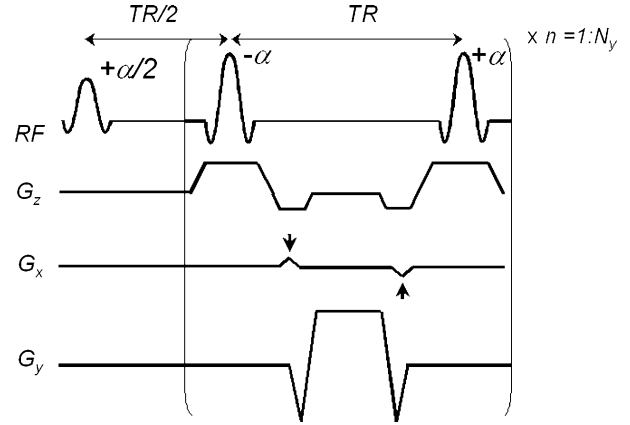

Fig. 1. Schematic diagram of the SSFP sequence used in the experiments and simulations.

(about the x-axis) and $\mathbf{R}_\pi(n)$ is the phase cycling matrix of the sense of rotation of the alternate α pulses (π radians about the z-axis) [16]. For fully balanced SSFP, TE = TR/2. The matrices are laid out explicitly below:

$$\mathbf{R}_\alpha = \begin{bmatrix} 1 & 0 & 0 \\ 0 & \cos\alpha & \sin\alpha \\ 0 & -\sin\alpha & \cos\alpha \end{bmatrix} \tag{3}$$

$$\mathbf{P} = \begin{bmatrix} \cos(2\pi\Delta f_0\tau) & \sin(2\pi\Delta f_0\tau) & 0 \\ -\sin(2\pi\Delta f_0\tau) & \cos(2\pi\Delta f_0\tau) & 0 \\ 0 & 0 & 1 \end{bmatrix} \tag{4}$$

$$\mathbf{C} = \begin{bmatrix} \exp(-\tau/T2(\tau)) & 0 & 0 \\ 0 & \exp(-\tau/T2(\tau)) & 0 \\ 0 & 0 & \exp(-\tau/T1) \end{bmatrix}. \tag{5}$$

The starting magnetization before the first α pulse was given by $M_s^- = \mathbf{PCR}_{\alpha/2}M_0$. Where $M_0 = [0, 0, M_0]$, is the initial starting magnetization, which is proportional to the product of the gas spin density and the optical pumping hyperpolarization level. The contribution to T_2 from the diffusion dephasing action of imaging gradients, was incorporated in the relaxation matrix, $\mathbf{C}$, by calculating the effective time-dependent transverse relaxation time, $T_2(\tau)$,

$$T_2(\tau) = \frac{\tau}{b(\tau)D + \tau/T_2}, \tag{6}$$

where τ represents the echo time, and T_2 is the upper limit on the transverse relaxation time for the given sequence as measured with a CPMG sequence with the same echo separation in the absence of gradient induced diffusion dephasing.

The relation in Eq. (6) is based on the approximation that diffusion dephasing due to the imaging gradients in fully balanced SSFP is described by an additional transverse relaxation term, $\exp(-b(\tau)D)$. Previous theoretical and experimental work has shown that this approximation can break-down for diffusion weighted SSFP (where the sequence is no longer fully balanced) in the limit where

either the diffusion-weighted gradient b-values are high or the diffusion coefficient is large [17–20]. The validity of this approximation for the fully balanced SSFP sequence used in the ^{3}He NMR regime is discussed later.

For gas phantoms $T_2 = 1$ s was assumed from observation of the signal decay in experiments with $\alpha = 180°$ where the SSFP sequence equates to a CPMG sequence with inter-echo time TR – see Section 2.2 and Fig. 3a of Results. For simulations of *in vivo* conditions a $T_2 = 100$ ms was assumed from values reported at 1.5 T by Vignaud et al. [21], which were also derived from a CPMG sequence, these are shorter than the estimates of Mugler et al. of several seconds [22]. For the simulations of a SPGR sequence, it was assumed that the phase and slice gradients were not balanced i.e. the phase dispersion due to the area under both slice and phase encode was not refocused. In this case the T_2 was replaced with $T_2^* = 25$ ms as measured previously at 1.5 T *in vivo* using multiple interleaved single gradient echoes [23]. The diffusion weighting b value, $b(\tau)$, was calculated from the time integral of the readout gradient waveform [8]

$$b(\tau) = \int_0^\tau |k(t)|^2 \, dt, \tag{7}$$

where $k(t) = \gamma \int_0^t G(t') \, dt'$. The same waveforms that were used in the experimental pulse sequences were used to calculate $b(\tau)$ as outlined in the experimental methods. It is worth noting at this point that in the start up period TR/2, there are no readout gradients applied and so the diffusion b value $= 0$.

Two versions of the sequence were simulated with different read gradient waveforms to assess the effects of diffusion dephasing. The b values for the two read gradient waveforms were, $b(\text{TE}) = 0.292$ s cm^{-2} and $b(\text{TR}) = 0.584$ s cm^{-2} for the high bandwidth waveform (referred to as the high b value sequence), and, $b(\text{TE}) = 0.0757$ s cm^{-2} and $b(\text{TR}) = 0.1514$ s cm^{-2} for the low bandwidth waveform (referred to as the low b value sequence). For both sequences, $\text{TE} = \text{TR}/2 = 5$ ms. The remaining parameters for the gas phantom simulations were, $T_1 = 20$ min and $D = 0.9$ cm^2 s^{-1} as measured previously in a plastic syringe. The parameters for the simulations of *in vivo* conditions were; $T_1 = 20$ s and $D = 0.2$ cm^2 s^{-1}. To account for B_0 inhomogeneity, the simulations could be performed assuming a Lorentzian distribution in the resonant frequency. The FWHM of the ^{3}He resonance was estimated from visual inspection of the shimmed spectrum. This then allowed an estimate of the T_2^* of the ^{3}He syringe phantom to be made (FWHM $\approx 1/\pi T_2^*$) resulting in $T_2^* = 100$ ms. To study off-resonance effects, the RF transmit center frequency f_0, was offset in 10 Hz increments between 0 and 60 Hz.

2.2. Experimental methods

2.2.1. Gas polarization

The ^{3}He gas (Spectra Gases, UK) was polarized on site to approximately 30% with rubidium spin exchange appa-

ratus (GE Healthcare, Durham, NC). NMR studies were performed using plastic syringes as phantoms, which were placed along the z-axis at iso-center. These contained 10 cm^3 of ^{3}He and 40 cm^3 of N$_2$. Further phantom imaging experiments were performed with read gradients on 1 l volume Tedlar plastic bag phantoms (Jensen Inert Products, Coral Springs, FL) which were filled with 100 cm^3 of ^{3}He and 900 cm^3 of N$_2$. The gas mixture for both phantoms had a measured apparent diffusion coefficient, $D = 0.9$ cm^2 s^{-1}. The longitudinal magnetization for the respective phantoms was estimated from $M_0 = \mu P N/2$, where μ is the nuclear magnetic moment of ^{3}He, N is the number of ^{3}He atoms in the volume and P is the polarization. For the syringe phantoms, $M_0 \sim 7 \times 10^{-7}$ J T^{-1}, for the bag phantom, $M_0 \sim 7 \times 10^{-6}$ J T^{-1}. Prior to placing the phantoms in the MRI scanner, their signal was measured on a low frequency (24 kHz) calibration spectrometer using a small surface coil with a small flip angle pulse-acquire sequence. This provides a means of measuring the relative M_0 of the sample prior to the experiment, thus allowing normalization for differences that may result from inaccuracies in gas volume dispensing and polarization decay in the optical pumping storage cell between experiments.

2.2.2. MRI

All experiments were performed on a 1.5 T whole body MRI system (Eclipse, Philips Medical Systems, Cleveland, OH). The system was fitted with a second RF amplifier (2 kW, Analogic Corporation, Peabody, MA) and transmit–receive circuit tuned to 48.5 MHz for ^{3}He. A home-built low-pass birdcage transmit–receive coil was used for all of the phantom work. The coil was shielded and had 12 elements with a length of 25 cm and diameter 18 cm. The measured Q with the coil matched inside the magnet was 250 at 48.5 MHz. Isolation between the two orthogonal ports was -26 dB. A flexible twin saddle design quadrature transmit–receive coil was used for all of the *in vivo* ^{3}He work (IGC Medical Advances, Milwaukee, WI).

A transmitter pulse angle calibration was first performed by acquiring a set of $n = 1{:}64$ FIDs with a pulse-acquire sequence with a short TR (4 ms). Any residual transverse magnetization between pulses was spoilt with a gradient crusher. The received ^{3}He signal from the whole of the coil was then fitted to $M_n = M_0 (\cos \alpha)^{n-1} \sin \alpha$, enabling an estimate of α to be made for the loaded coil. For the phantom calibration, 10 cm^3 of gas diluted with 990 cm^3 of N$_2$ was used. For *in vivo* calibration, 30 cm^3 of gas diluted with 970 cm^3 of N$_2$ was used. The residual longitudinal magnetization was then used to center the resonant frequency and shim the subject/phantom by manual adjustment of the linear x, y and z shim currents. Following shimming an estimate of the FWHM of the linewidth of the spectrum was made.

2.2.3. SSFP sequence

The 2D SSFP sequence was programmed in-house. Due to spectrometer constraints the sequence had a relatively

long TR = 10 ms, when compared to many SSFP sequences currently in use on high performance gradient systems with rapid sampling rates. Two variants of the sequence were used with high and low *b*-value readouts. The high *b*-value (BW = 250 kHz) version was used for investigations of SSFP in gas phantoms in order to assess the effects of diffusion dephasing. The readout gradient waveform for this sequence had linear ramps, a constant gradient during sampling = 16.6 mT m^{-1}, 256 samples and a dwell time of 4 µs. The low *b*-value version (BW = 62.5 kHz) was used for SSFP imaging to reduce diffusion dephasing. The readout gradient waveform for this sequence had linear ramps, a constant gradient during sampling = 4.2 mT m^{-1}, 128 samples and a dwell time of 16 µs. The *b*-values of both waveforms are given in Section 2.1.

2.2.4. Phantom NMR experiments

A set of NMR experiments was performed on phantoms without any imaging gradients to investigate the SSFP signal dynamics in the limit of long effective T_2 where diffusion dephasing is limited to the non-refocused contribution from the background field inhomogeneity gradients. These NMR experiments were performed without slice selection to ensure signal change due to mixing of gas polarization by diffusion in and out of slice was eliminated as a source of error from the analysis of the signal time course [6]. In the first series of experiments on the same phantom, a wide range of flip angles were studied, $\alpha = 10$–192°. Off-resonance effects were investigated in a second series of experiments, which took place on the same phantom with a fresh supply of polarized ^{3}He. In these experiments, the spectrometer frequency was offset between experiments in 10 Hz increments in the range $\Delta f = 0$–60 Hz. In both these series of NMR phantom experiments, the diminishing polarization between measurements on the same sample was monitored with a single pulse acquire with a small flip angle of 0.5°. This allowed normalization of the data for M_0 for direct comparison.

2.2.5. Phantom MRI experiments

The relative SNR and filtering of the k_y direction (phase encode) of *k*-space with SSFP was investigated by turning off the phase encode and slice gradient and running the high *b*-value sequence with read gradients alone in a 1D imaging experiment. Direct comparisons were then made with the optimized SPGR version of the same sequence. 2D phantom imaging was then performed using the low *b*-value SSFP sequence with a 10 mm axial slice with α in the range 5–45° and $N_y = 128$ phase encode views. Between imaging experiments, the depolarized gas in the imaged slice was allowed to mix by diffusion with the rest of the gas in phantom for 2 min before the signal from the whole phantom was calibrated for residual M_0 as described above. The same slice was also re-imaged with the SPGR sequence for comparison. This was the same sequence with the exception that, there was no ($\alpha/2 - TR/2$) startup, and spoiling was achieved by removing the read gradient refo-

cus lobe and placing a crusher gradient on all axes. The SPGR sequence had an optimum $\alpha = 8°$ to provide maximum weighting of $k_y(0)$ for $N_y = 128$ sequential phase encode views [8].

2.2.6. In vivo MRI experiments

All of the *in vivo* imaging experiments were performed with a 2D slice thickness of 13 mm, 128 sequential phase encodings and a FOV = 48 cm. The studies were conducted on three healthy volunteers (Subject 1: male, 36 y, 100 kg; Subject 2: male, 24 y, 80 kg; Subject 3: male, 35 y, 80 kg) with informed consent and approval from the local Research and Ethics Committee. The imaging was performed in a single breath-hold following inhalation from a Tedlar bag filled with 300 cm^3 of ^{3}He and 700 cm^3 of N_2. A range of flip angles were studied, $\alpha = 5$–20°. Higher flip angles were difficult to achieve *in vivo* due to power constraints of the RF amplifier (2 kW) and imperfect matching of the flex coil, the loading of which changed significantly with subject size.

3. Results

3.1. Phantom NMR experiments – 10 cm³ of ³He and 40 cm³ of N₂ in plastic syringes

Fig. 2 shows the SSFP results from the syringe phantom NMR experiment using a flip angle $\alpha = 30°$.

All curves are normalized by the signal from the first α RF pulse. The rapid stabilization of the signal into a steady-state, indicates that in the absence of read gradients, and with good B_0 homogeneity, SSFP can offer almost complete refocusing of transverse magnetization. The stabilized signal for points $n > 10$ is almost completely flat compared to the SPGR signal with the same flip angle. The SSFP signal response is also much flatter than that of the optimum SPGR sequence with $\alpha = 8°$ for $N_y = 128$
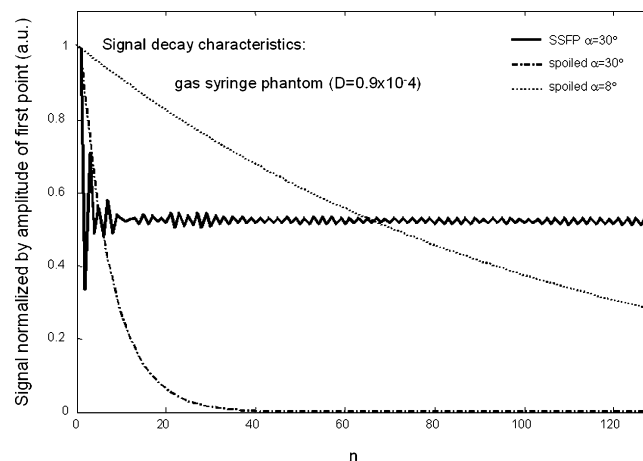

Fig. 2. SSFP signal decay for a gas syringe phantom acquired on-resonance with $\alpha = 30°$ flip angle over 128 views. The curves are normalized by the signal from the first α RF pulse. Also shown is the SPGR signal decay for $\alpha = 30°$ and the optimum $\alpha = 8°$.

views, which would impart more k_y filtering and broadening of the PSF in an imaging experiment. Despite the normalized curves passing through the $n = 64$ point (center of k_y space in the equivalent MRI experiment) around the same place, the SSFP sequence has a higher weighting than the SPGR version, which is given by the ratio: $\sin(\alpha_{ssfp}/2)/$ $(\sin\alpha_{spoil}(\cos\alpha_{spoil})^{n-1})$ in the absence of diffusion weighting [8]. This gives a relative predicted SNR improvement of over 3.

3.2. SSFP NMR—flip angle dependence

Fig. 3 shows the results from the flip angle experiments performed in syringe phantoms. The curve shapes in Fig. 3a are very similar, with a rapid approach to a steady-state. These experiments were performed in succession over a 10-min period on the same phantom. Therefore a reduction in the starting magnetization, M_0, between experiments was to be expected due to incomplete refocusing of the steady-state signal and T_1 decay (T_1 of $^3He/N_2$ mix $\approx$20 min inside the syringe). The depletion in M_0 between experiments was normalized by using the pulse-acquire signal intensity as described in the Methods. In Fig. 3b the normalized amplitude of the $n = 64$ view is plotted against flip angle. The data shows a good fit to the $\sin(\alpha/2)$ curve of theory as depicted by the solid line.

3.3. SSFP NMR—off-resonance behaviour

Fig. 4 shows the results of the SSFP experiments performed at increasing frequency increments off-resonance. The curves display harmonic beating in the SSFP signal as Δf increases to 50 Hz as shown in Fig. 4a. These experiments were also performed on the same syringe phantom in succession, which explains the decreasing signal intensity with increasing Δf. A more direct comparison can be made, by scaling the curves by division with the magnitude of the first point. Fig. 4b shows the on-resonance curve and the 50 Hz off-resonance curve scaled in this manner. Off-resonance introduces beating, which causes the banding artifacts common in ^1H SSFP images and also compromises the efficiency of refocusing of the magnetization when compared to the on-resonance signal, which soon stabilizes to a slowly decaying curve.

The curves of Fig. 4c were simulated based upon estimates of the relaxation times and frequency dispersion in the phantom from the FWHM of the spectrum (3.2 Hz) and show a good resemblance to experiment (Fig. 4b).

3.4. Phantom MRI experiments—100 cm³ of ³He and 900 cm³ of N₂ in Tedlar plastic bag

3.4.1. SSFP MRI—flip angle dependence

Fig. 5 demonstrates the flip angle dependence of the efficiency of the SSFP sequence in the presence of read gradients; the experimental curves (shown in blue) are scaled by the magnitude of the first point. Also shown are the
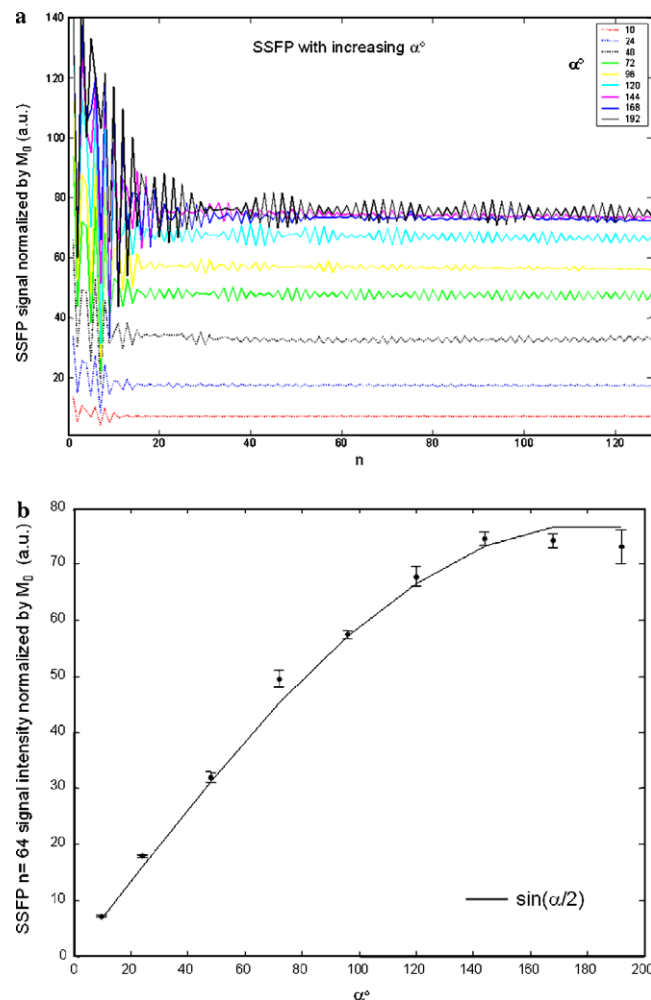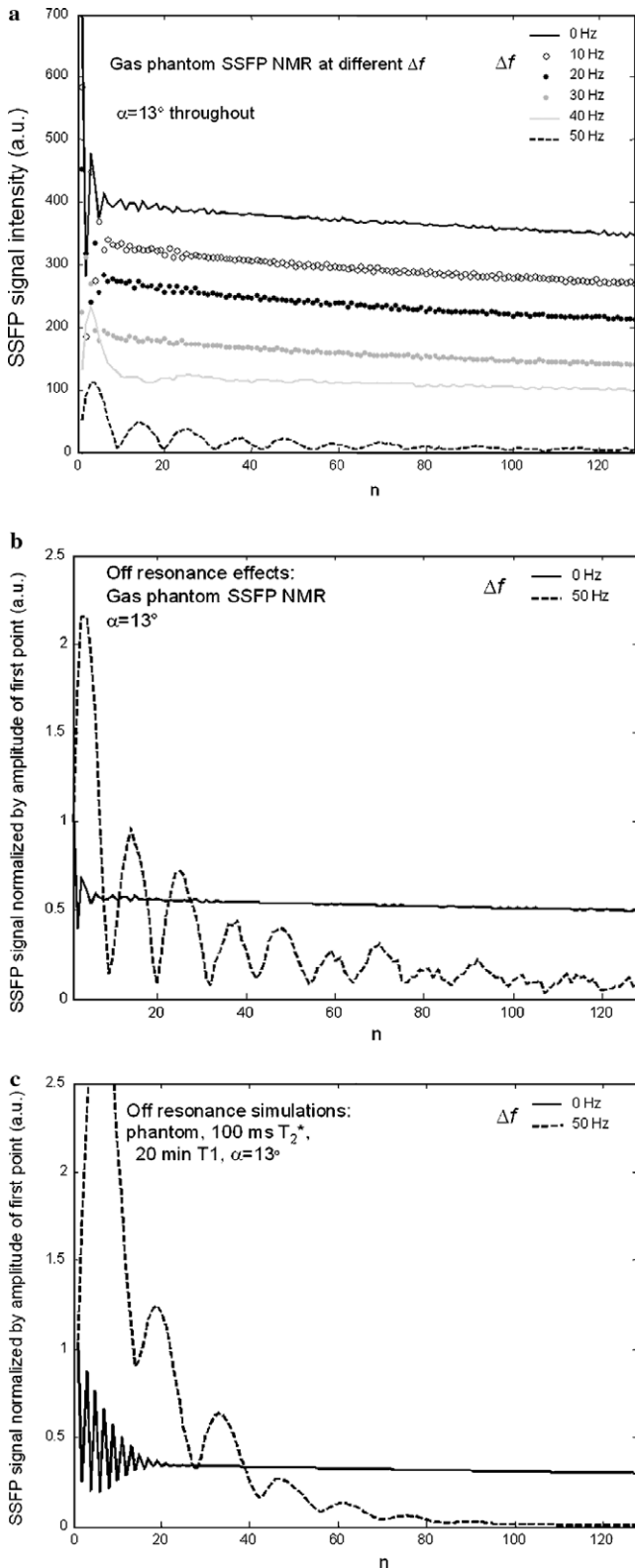
Fig. 3. (a) SSFP signal decay from a gas syringe phantom acquired on-resonance with different flip angles. The same gas phantom was imaged successively with an increasing flip angle in the range $\alpha = 10$–192°. The curves have been normalized by the amplitude of the starting magnetization (M_0) as measured with the pulse-acquire sequence. All curves share the same feature of a flat underlying steady-state with different levels of oscillation. (b) Curve of the flip angle dependence of the signal. Signal intensity was measured as the amplitude of the $n = 64$ point, after M_0 normalization with amplitude of the FID from the pulse acquire sequence. The error bars were calculated from the SD of the oscillation in the 10 points either side. The error bars get larger as the oscillations become larger at higher flip angle and also as noise starts to become evident in the steady-state signal at higher flip angle due to a decreasing M_0. The data shows a good fit to the $\sin(\alpha/2)$ curve of theory plotted as a solid line.

simulated curves for $\alpha = 15°$ (grey solid line) and 30° (grey dotted line). The simulations accounted for the effects of diffusion, with an effective $T_2 = 18.67$ ms which was calculated from Eq. (6), for; TE = 5 ms, $b = 0.292$ s cm^{-2}, $T_2 = 1$ s, $D = 0.9$ cm^2 s^{-1} and zero frequency offset. The curves, which were also scaled by the magnitude of the first point, show a similar shape to those observed experimentally; however it is obvious from the different vertical range of the curves, that the experimental data demonstrates a smaller first point than those predicted by the simulations. When the simulations were corrected for the effects of radi-

ation damping, a better match with experiment is seen in the black lines.

The inset of Fig. 5b demonstrates the effect of including an intrinsic frequency distribution, with simulations for a 1 and 10 Hz line broadening. The frequency distribution smoothes out some of the initial oscillations, but both curves then stabilize to the same shape.
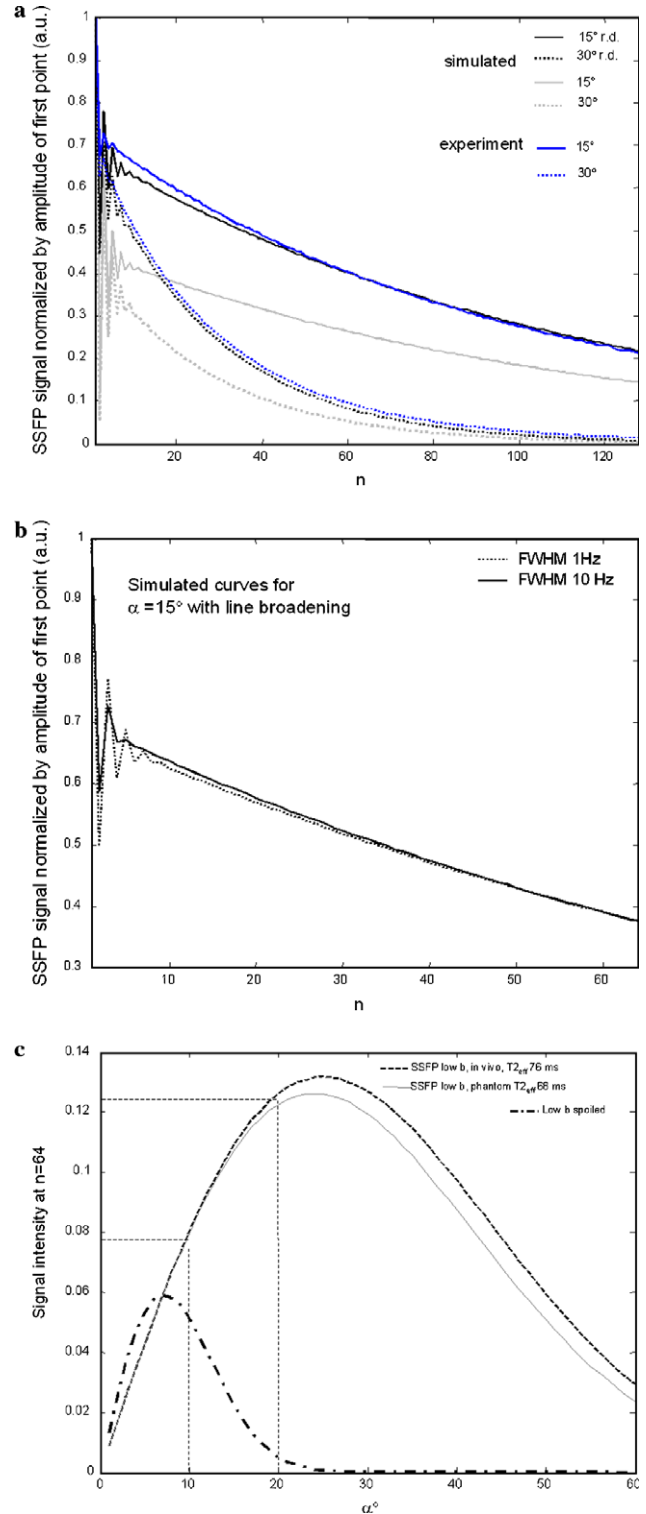

Fig. 4. (a) SSFP signal decay for a gas syringe phantom as the resonant frequency is offset in regular increments Δf. All off-resonance experiments were performed with $\alpha = 13°$ in succession on the same phantom. These curves were deliberately not normalized by the M_0 in order to separate them in the vertical range. Harmonic beating in the SSFP signal is evident as Δf increases to 50 Hz. (b) The on-resonance curve and the 50 Hz off-resonance curve scaled by the amplitude of the respective first points. (c) Simulated scaled curves.
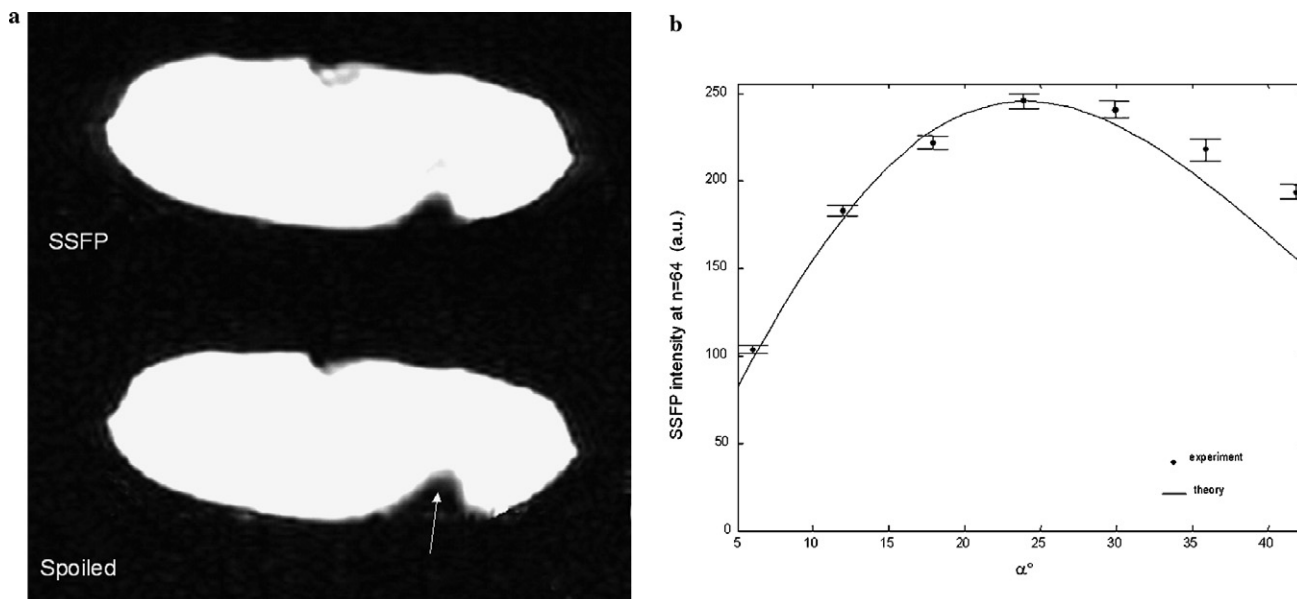
Fig. 6. (a) Axial 2D SSFP image acquired with the low b-value readout from a 10 mm slice from a Tedlar bag phantom with the optimum flip angle of $\alpha = 24°$, and 128 phase encodings. Slight off-resonance banding is visible near the fold in the flexible bag where the susceptibility gradients are greatest. Shown below is the axial SPGR image acquired from the same 10 mm slice with the optimum flip angle of $\alpha = 8°$, and 128 phase encodings. The arrow indicates the greater degree of signal dephasing in the SPGR image in the region of susceptibility related field inhomogeneity near the fold in the bag. (b) SNR of the 2D phantom imaging experiments using the low b-value sequence at a range of flip angles. The SNR, which was measured from the magnitude images, was normalized for M_0 decay between successive imaging experiments by division with the amplitude of the low flip pulse-acquire FID. The simulations shown are the weighting of the $n = 64$ echo for the low b-value sequence with an effective $T_2 = 68$ ms–see grey curve of Fig. 5c. The experiment and theory show good agreement, particularly at lower α.

Fig. 5c shows simulations of the weighting of the $k_y(0)$ point ($n = 64$) for sequentially encoded SPGR and SSFP acquisitions as a function of the flip angle for different effective T_2. The dashed line is that predicted for the low b-value gradient with an *in vivo* $T_2 = 100$ ms and $D = 0.2$ cm^2 s^{-1} giving an effective T_2 value of 76 ms. The optimum predicted $\alpha = 25°$. The dotted line is that predicted for the phantoms with the low b-value gradient (effective T_2 68 ms), the optimum predicted $\alpha = 24°$. The dash-dot line shows the simulated SPGR signal behaviour for *in vivo* conditions. This was based on a $T_2^* = 25$ ms [23], optimum $\alpha = 8°$ and the same degree of diffusion dephasing as the SSFP waveform at $\tau = \mathrm{TE} = 5$ ms, giving an effective $T_2^* = 20$ ms.

The results of the gas phantom images acquired with the low b-value SSFP sequence are shown in Fig. 6 with a direct comparison with the SPGR image of the same 10 mm axial slice. The SSFP image, demonstrates a small off-resonance banding artifact close to the fold at the top of the phantom. However the signal dephasing due to field inhomogeneity in the SPGR image (bottom arrow) is refocused to some extent in the SSFP image. Otherwise the spa-

tial resolution and uniformity are comparable with those observed with the SPGR image from the same slice. The SNR of the SSFP image (SNR = 71) is 1.5 times that of the SPGR after it has been scaled for depolarization (normalized SNR = 46). The simulations of Fig. 5c, predict a twofold increase in optimum SNR of SSFP (grey line) compared to SPGR (dash-dot line). When the SSFP SNR was investigated as a function of flip angle, a very good agreement with theory was observed for the 1D imaging experiments (single readout gradient), especially at lower α, as is shown in Fig. 6b.

3.4.2. SSFP MRI in vivo

Fig. 7 shows the *in vivo* SSFP signal response from the whole of the lungs of Subject 1 with $\alpha = 14°$, both with and without the high b-value read gradients applied.

Figs. 8a and b are axial images acquired from Subject 1 with the low b-value SSFP sequence with $\alpha = 20°$, the images are sharp with well-defined edges and very little blurring. This is further evidence of the reduced weighting of the k-space filter that can be achieved at high flip angles

Fig. 5. (a) 1D SSFP imaging experiments performed on the bag phantom with read gradients applied. The SSFP signal decay is shown at $\alpha = 15°$ (dotted blue line) and 30° (solid blue line) flip angle. The simulated SSFP signal decay curves are also shown, the grey curves do not include the effects of radiation damping. The black curves are those simulated with the effect of radiation damping. (b) Simulations of the same $\alpha = 15°$ SSFP curves in the range $n = 1$:64 to illustrate the effect of background B_0 inhomogeneity. The curves shown were simulated with a 1 and 10 Hz Lorentzian frequency distributions centered around zero. The high frequency oscillations in the initial phase are damped by the frequency distribution. (c) Simulations of the flip angle dependence of the SSFP and SPGR sequences for *in vivo* parameters. Simulations for SSFP were performed with effective $T_2 = 68$ ms (low b-value phantom) and 76 ms (low b-value *in vivo*) as derived from Eq. (6) for the *in vivo* imaging parameters. The faint dashed lines indicate the predicted signal intensities of SSFP imaging at the flip angles that were used in the *in vivo* imaging investigation of the effect of flip angle–see Figs. 8e and f for the results.
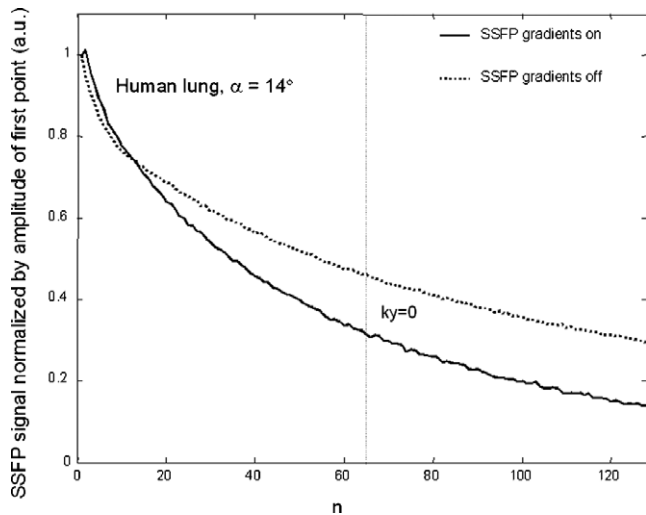
Fig. 7. SSFP signal dynamics *in vivo*, the results were acquired from Subject 1 with $\alpha = 14°$. The efficiency of refocusing in SSFP (dotted line) is reduced when compared to the results from the gas phantoms shown in Fig. 3a. The application of a readout gradient (solid line) further reduces the effective T_2 by diffusion dephasing.

with the sequentially encoded SSFP sequence as was demonstrated in Fig. 7. The off-resonance banding artifacts, previously observed by Mugler et al. [13] in coronal images, were observed here only in the slice closest to the diaphragm – see arrow in Fig. 8b. Fig. 8c is a coronal SSFP image from Subject 2 with $\alpha = 20°$, the image is not blurred with delineation of the vessels and sharp delineation of the edges of the lungs. Off-resonance banding artifacts are evident near the diaphragm. Fig. 8d is the corresponding SPGR image acquired with the optimum flip angle of 8° for 128 views with sequential encoding (see dash dot curve of Fig. 5c). Although free from off-resonance banding artifact, the SNR of the SPGR image is less than that of the SSFP image. The SNR was compared over all slices by

averaging the SNR from six ROI's, placed in the upper, mid and lower, left and right lungs. SSFP demonstrated a higher SNR (SSFP SNR = 10.3, SPGR SNR = 8.8). This increase in SNR is less than was predicted by the simulations of Fig. 5c which predict a twofold higher weighting of the center of *k*-space for SSFP with $\alpha = 20°$ compared to the SPGR. Figs. 8e and f are coronal SSFP images from the same slice from Subject 3, acquired with $\alpha = 10°$ and $\alpha = 20°$, respectively. The images have been windowed to the same contrast and brightness levels to emphasize the higher SNR in the $\alpha = 20°$ image (1.6 times higher) than in the $\alpha = 10°$ image.

4. Discussion

4.1. SSFP NMR—flip angle dependence

The $\sin(\alpha/2)$ relation of Fig. 3b has been observed previously, with solutions of HP ^{13}C compounds that had very long T_1 and T_2 [12], and relies on almost complete refocusing of the transverse coherence to enable efficient exchange with the longitudinal magnetization. This was possible in these ^{3}He NMR experiments due to the fact that the T_1 is long (20 min) and the T_2 is also relatively long ($\sim$1 s) in the absence of diffusion dephasing. It is worth pointing out that the optimum flip angle of $\alpha = 180°$ as observed by Svensson et al. with HP ^{13}C [12], results from the long T_2, and indeed in this case the SSFP sequence that uses a $(\alpha/2 - TR/2)$ starter equates to a CPMG NMR sequence or a single shot multiple spin echo imaging sequence.

4.2. SSFP NMR – off-resonance behaviour

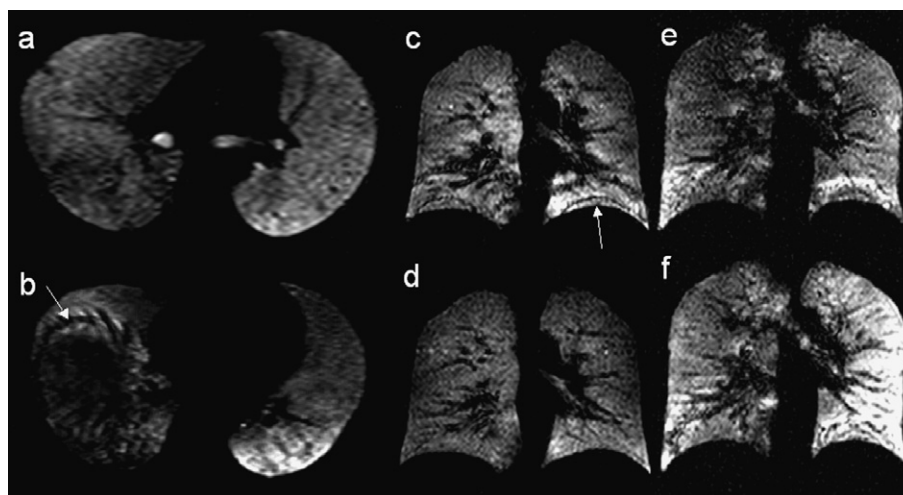The characteristic harmonic beating at offset frequency 50 Hz is evident in the SSFP signal. With TR = 10 ms,

Fig. 8. Axial SSFP images acquired with $\alpha = 20°$ from Subject 2, the images are sharp with well-defined edges and very little blurring. Off-resonance banding artifacts were only observed in the slice closest to the diaphragm – see arrow in (b). (c) A coronal SSFP image acquired with $\alpha = 20°$ from Subject 3. (d) The SPGR image from the same slice acquired with the same volume of gas. (e and f) Coronal SSFP images from the same slice from Subject 2, acquired with $\alpha = 10°$ and $\alpha = 20°$, respectively. SNR increases with α without a noticeable change in the level of blurring.

an off-resonant frequency of 100 Hz would give a full 2π phase precession during TR. The frequency range investigated thus represents the response for just over half of a full periodic cycle and the beating of the 50 Hz offset signal is due to anti-phase interference. It is evident that the on-resonance data in Fig. 4a shows less efficient refocusing than the data in Fig. 3a, which has a flat steady-state. This may be due to a poorer shim for this experiment–FWHM 3.2 Hz whereas line-widths <2 Hz have been achieved previously in syringe experiments.

Differences in simulated and experimental curves in Figs. 4b and c are attributed to inaccuracy in estimates of the actual frequency distribution in the phantom and imprecision in experimental center frequency measurement. Hargreaves et al. [15] noted similar discrepancies between simulated and experimental results with ^{1}H SSFP, and also attribute them to inexact knowledge of the experimental frequency distribution. For the motionally narrowed regime of freely diffusing gas the Lorentzian distribution is the most appropriate approximation. Another possible source of difference is the estimate of the T_2. For gas phantoms this was assumed to be $T_2 = 1$ s, which is a conservative lower limit based on the rate of decay of the SSFP signal at $\alpha \approx 180°$ as shown in Fig. 3a. The T_2 dependence means that the observation of the SSFP signal response could be one way of determining the [3]He T_2 for the given pulse sequence parameters in a way similar to that proposed by Oregioni et al. for thermally polarized [129]Xe [24].

4.3. SSFP MRI – flip angle dependence

Comparing Fig. 5a with Fig. 3a it can be seen that the application of imaging readout gradients shortens the effective T_2 due to diffusion dephasing, and reduces the efficiency of SSFP with increasing flip angle compared to the NMR experiments. Nevertheless, these phantom experiments highlight the potential improvements over the SPGR signal behaviour (Fig. 2) providing that effective T2 > TR. For example the $\alpha = 15°$ SSFP data shows a comparable k_y filter function with an increase in SNR predicted by the ratio $\sin(\alpha_{\text{ssfp}}/2)/(\sin \alpha_{\text{spoil}}(\cos \alpha_{\text{spoil}})^{N_y/2-1}) = 1.7$. If effective T2 starts to approach T2* then the predicted SNR gains will be less.

Referring to the curves of Fig. 5a it is apparent that the experimental data demonstrates a smaller first point than those predicted by the simulations. An explanation for this difference is radiation damping of the large initial magnetization when it is first tipped in to the transverse plane by the first RF excitation ($\alpha/2$). The transverse magnetization following the first $\alpha/2$ pulse is not dephased as rapidly as in the subsequent inter-pulse periods because there are no readout gradients applied. The result is a highly coherent large transverse magnetization (resulting from the hyperpolarization) which induces a current in the coil, and sets up a counter field to the B1 [25]. The net effect is a 'pushing back' of some of the transverse magnetization in to the longitudinal direction prior to the application of the first α

pulse, which can be effectively treated as a lower than expected effective flip angle $<\alpha/2$ in the start-up phase. This effect has been observed previously in phantoms of HP gas with small receive coils of high Q [26]. A full description of the diagnosis of radiation damping in hyperpolarized NMR and the electromagnetic theory of the interaction for the birdcage resonator was recently presented [27] and will be submitted to this journal in the near future. For the purposes of this work the effect was accounted for by reducing the flip angle of the first rotation to 2/3 of its expected value i.e. $\alpha/3$. This is consistent with the flip angle calibrations observed with a radiation damping sensitized RF calibration sequence [27] for the transverse magnetization evolution periods experienced here. The resulting scaled curves ($\alpha = 15°$ black solid line and 30° black dotted line) closely resemble those observed experimentally. It is worth pointing out that the syringe phantom NMR experiments are not noticeably affected by radiation damping due to the fact that the starting M_0 was much smaller (1/10th volume of HP [3]He) and the sample-coil filling factor, η, is much less due to the phantom's smaller volume (50 cm³ compared to 1 l). The radiation damping relaxation time is proportional to $(QM_0\eta)^{-1}$ [25–27], as such the effect is negligible in small volume, low M_0 samples. Similarly the low Q of the loaded body coil and the shorter T_2^* of [3]He in lungs should eliminate radiation damping effects in *in vivo* SSFP.

4.4. SSFP MRI – diffusion effects on image SNR as a function of flip angle

The simulations of Fig. 5c demonstrate that higher SNR could be achieved with a higher flip angle if the time dependent diffusion attenuation term can be minimized through gradient optimisation [22]. Out of interest the reader is referred to Fig. 1 in the paper of Wu and Buxton [19], where experiments are described with diffusion weighted SSFP in liquids, and a flip angle dependence in the transverse magnetization as a function of diffusion was evident. The need for readout gradients with low b-values in order to preserve effective T_2 and hence SNR, ultimately imposes a limit on the maximum duration of the readout in [3]He SSFP MRI. It also limits the maximum read gradient and readout bandwidth possible, and therefore the minimum sequence TR. This is unlike the case of proton SSFP, where the *in vivo* sequence efficiency is greatest with ultra-short TR and high bandwidth readouts [28]. When diffusion dephasing can be mitigated, for example in HP [3]He NMR experiments that do not use imaging gradients, the corresponding curves are shifted to the right with a peak at $\alpha = 180°$ in the limit of negligible diffusion (curve of Fig. 3b), and the SSFP sequence becomes a CPMG sequence. This corresponds to the $\sin(\alpha/2)$ dependence of the transverse magnetization as observed with HP [13]C [12]. Ultimately, diffusion in the presence of background field inhomogeneity prevents complete refocusing and limits the measured T_2 to a value lower than the true dipole–

dipole upper limit. This incomplete refocusing is caused by the finite RF pulse separation in the echo train. Higher flip angles would be possible with SSFP MRI of HP [129]Xe, which has a lower sensitivity to diffusion dephasing due to its lower *in vivo* ADC [29]. Another suitable application would be high SNR HP SSFP [129]Xe spectroscopic imaging, where the *b*-values of the 2D phase encoding gradients are negligible [8] and diffusion dephasing is therefore minimal.

These simulations assumed a contribution to the effective T_2 from diffusion in SSFP that is described by an additional transverse relaxation term, $\exp(-b(\tau)D)$. Previous work with ^{1}H SSFP has shown that this approximation can break down in the limit where either the diffusion-weighted gradients are high, or the diffusion coefficient is large [17–20]. Under these conditions, the curve of log signal intensity versus *b*-value can deviate from linear – see Fig. 3 of [17] and Fig. 9 of [19]. The experiments described in [17–20] were performed with additional pulsed diffusion gradients either side of the α pulses for diffusion sensitization, and as such the SSFP sequences used were not fully balanced in terms of gradient waveform area. The time integrals of the imaging gradients simulated and used in this work with [3]He average to zero within a TR and are thus fully balanced. Further more the *b*-values representing diffusion during the frequency readout are weak when compared to those used in the diffusion weighted experiments described in [19], namely 10 mT m^{-1} gradients of 30 ms duration separated by 60 ms ($b = 3.2 \times 10^4$ s cm^{-2}). However the diffusion coefficients of liquids used in these experiments were characteristically lower than [3]He in air by between four to five orders of magnitude: phantom $D_{3He} = 0.9$ cm^2 s^{-1}, lung $D_{3He} = 0.2$ cm^2 s^{-1} compared to $D_{H_2O} = 2.5 \times 10^{-5}$ cm^2 s^{-1}. This gives a diffusion weighted attenuation approximation $\exp(-bD) = 0.45$ for the experiments described in [17] when compared to 0.77 for the high *b*-value [3]He bag phantom imaging experiments and 0.98 for the low *b*-value *in vivo* experiments described here. From these comparisons it is fair to conclude that the assumption of $\exp(-bD)$ for diffusion related T_2 relaxation is valid *in vivo* however the approximation may become less valid for free gas experiments with higher *b*-values. These effects may therefore also contribute to the differences between simulation and experiment in the imaging experiments of Fig. 5a after correction for radiation damping was made. This is the subject of further work where non-linearity in the diffusion dependence of HP [3]He SSFP will be explored at higher *b*-values.

When the SSFP SNR was investigated as a function of flip angle, a very good agreement with theory was observed for the 1D imaging experiments (single readout gradient), especially at lower α, as is shown in Fig. 6b. With respect to the 2D phase encoded images presented in Fig. 6a, the shortfall of experimental SNR results with theory predicted in Fig. 6b could be due to distortion in the slice profile causing a non-ideal flip angle response [8] or inter-slice polarisation mixing between α pulses on successive phase encode views, which was analyzed in detail previously for

2D SPGR sequences [6]. These mechanisms are currently under further investigation. The effects due to the second possible explanation are expected to be less significant *in vivo* by virtue of the lower ADCs.

4.5. SSFP MRI in vivo

With regard to the *in vivo* SSFP signal dynamics shown in Fig. 7, the coil has quite a poor B1 homogeneity; the standard deviation in flip angle across the whole of the lungs has been previously measured as approximately $\pm 50\%$ [30]. Furthermore there is significant B_0 inhomogeneity across the lungs. These two factors explain why the well-defined oscillatory behaviour of the SSFP signal that was observed in the phantom experiments (which had a homogeneous volume B_0 and B_1), is absent in the *in vivo* curves (dotted line). Nevertheless, the k_y filter is similar in shape to that of the optimum SPGR sequence shown in Fig. 2 with approximately twofold higher weighting in SNR. The application of the high *b*-value readout gradient (solid line) reduces the effective T_2 of [3]He in the lungs and reduces the efficiency of SSFP as was observed in the results from the gas phantoms. The SNR should improve with a higher flip angle of $\alpha = 25°$ as demonstrated by the simulations of Fig. 5c, but the short effective T_2 compromises the spatial resolution by broadening the PSF at very high flip angles as was found in the phantom MRI experiments. Therefore the SNR $\propto (\sin \alpha/2)$ relation shown in Fig. 3b and reported by Svensson et al. with HP ^{13}C is not valid for SSFP imaging of [3]He in the lungs if blurring in the images is to be avoided. The flip angle of 70° reported by Mugler et al. [13] was performed with a sequence with *b*-value of 0.046 s cm^{-2}. This flip angle would certainly have produced a heavily broadened PSF with the gradient configuration described in this work. As no mention of the effect of flip angle on relative spatial resolution was made in their work a direct comparison is not possible. The simulations for the gradient configuration presented, indicate an optimum *in vivo* flip angle of around 25°. In this work, higher *in vivo* flip angles were not possible with the flex coil used due to the present RF power limitations. However the phantom imaging experiments that were performed with read gradients, (Fig. 6b), fully indicate that the signal curve becomes more heavily weighted at higher α due to incomplete refocusing of transverse coherence.

With regard to the *in vivo* SNR comparisons of SSFP and SPGR in Fig. 8, as in the phantom experiments, the shortfall of experimental results with the simulations (performed on-resonance) is attributed to off-resonance and line broadening effects caused by B_0 inhomogeneity, which is high in the lungs. Reduction in refocusing efficiency by slice mixing through diffusion may also contribute to the shortfall but is expected to be less of a contributing factor than in the phantom imaging experiments. A slight further increase in SNR may be found at the optimum *in vivo* flip angle of $\alpha = 25°$ which was not achieved in practice due to power constraints of the RF amplifier and imperfect

matching of the flex coil. The SNR comparison of the *in vivo* images shown in Figs. 8e and f, is in good agreement with the simulated data and is highlighted by the faint dashed lines in Fig. 5c. Despite the increased flip angle both images display comparable spatial resolution indicating that the level of PSF broadening through the k-space filtering effect at higher flip angle is acceptable.

Although the SSFP images show higher SNR, their diagnostic utility at high B_0 remains to be verified, largely because of the prevalence of banding artifacts, which may be misdiagnosed as ventilation defect as has been described previously for SPGR images in regions of field inhomogeneity [31,33]. The robust nature of optimized SPGR sequences make choice of SSFP over SPGR for routine clinical use a difficult one. In this work, variable flip angles [7] were not used with SPGR due to spectrometer pulse programming constraints so it is hard to say how SSFP performs against fully optimized SPGR. The SSFP sequence has yet to be used for routine breath-hold imaging on this system as the benefits of increased SNR are compromised by the banding artifacts which could be misdiagnosed as ventilation defect.

These artifacts could be further mitigated by refined shimming methods, reducing the sequence TR with a higher performance system, or alternatively by performing HP ^{3}He SSFP imaging at lower B_0 [11,26,32–34]. The high diffusivity of ^{3}He and the associated shortening of T_2 due to gradient dephasing, precludes the use of very high flip angles previously reported for SSFP HP ^{13}C MRI [12]. Moreover care should be taken not to degrade SNR in HP ^{3}He SSFP through excessive T_2 shortening through the use of sequences with strong readout gradients and high bandwidth that are now standard in short TR proton SSFP sequences.

Higher SSFP sequence efficiency through use of higher α is expected with ^{129}Xe MRI by virtue of the lower *in vivo* diffusion coefficient. However, the higher optimum α that is expected could create potential SAR problems with the use of high α SSFP at short TR, which are already an issue *in vivo* with ultra-short TR ^{1}H SSFP. Providing the effective T_2 can be kept short with gradient optimization, HP ^{3}He SSFP has the potential for larger 2D phase encoding matrix sizes than is achievable with SPGR sequences and possibly 3D SSFP experiments. These experiments were performed with sequential phase encoding throughout. Centric encoding would be inadvisable due to the oscillatory nature of the signal in the stabilization period as it approaches steady-state ($n < 10$). Alternatively a preparatory scan phase could be used in which data was not collected as the signal approaches a pseudo-steady state, followed by sampling with centric or half-Fourier sequential encoding.

5. Conclusion

It has been demonstrated theoretically and experimentally that SSFP sequences can provide high spatial resolu-

tion images of lung ventilation at breath-hold with HP ^{3}He at 1.5 T with the potential for higher SNR than SPGR methods. Although HP gas M_0 is not renewable, under the right conditions of a long effective T_2, a pseudo-steady-state can be achieved within the time course of an MR imaging experiment. When effective T_2 is shortened by diffusion dephasing, SSFP yields a decaying magnetization response. Nevertheless this non-steady-state can still be used to good effect *in vivo* as it provides higher SNR for a given level of blurring in the PSF than an optimized SPGR sequence response.

The theoretical analysis presented here, fully encompasses the effects of a finite polarization and a time-dependent diffusion dephasing effect of the encoding gradients. This work represents an extension of the matrix methods presented in the past [15,16,18,19] for SSFP of thermally polarized proton spins to the analysis of HP gas signal dynamics. Furthermore the simulations presented accurately account for off-resonance effects that were not included in the analytical analysis of the HP ^{13}C signal previously presented by Svensson et al. [12].

References

[1] B.M. Goodson, Nuclear magnetic resonance of laser-polarized noble gases in molecules, materials, and organisms, J. Magn. Reson. 155 (2002) 157–216.

[2] H.E. Moller, X.J. Chen, B. Saam, K.D. Hagspiel, G.A. Johnson, T.A. Altes, E.E. de Lange, H.U. Kauczor, MRI of the lungs using hyperpolarized noble gases, Magn. Reson. Med. 47 (2002) 1029–1051.

[3] H. Middleton, R.D. Black, B. Saam, G.D. Cates, G.P. Cofer, R. Guenther, W. Happer, L. Hedlund, G.A. Johnson, K. Juvan, J. Swartz, MR imaging with hyper-polarized 3He Gas, Magn. Reson. Med. 33 (1995) 271–275.

[4] P. Bachert, L.R. Schad, M. Bock, M.V. Knopp, M. Ebert, T. Grossmann, W. Heil, D. Hofmann, R. Surkau, E.W. Otten, Nuclear magnetic resonance imaging of airways in humans with use of hyperpolarized 3He, Magn. Reson. Med. 36 (1996) 192–196.

[5] E. de Lange, J. Mugler, J. Brookeman, J. Knight-Scott, J. Truwit, C. Teates, T. Daniel, P. Bogorad, G. Cates, Lung air spaces: MR imaging evaluation with hyper-polarized He gas, Radiology 210 (1999) 851–857.

[6] J.M. Wild, N. Woodhouse, M. N Paley, S. Fichele, Z. Said, L. Kasuboski, E.J. van Beek, Comparison between 2D and 3D gradient-echo sequences for MRI of human lung ventilation with hyperpolarized 3He, Magn. Reson. Med. 52 (2004) 673–678.

[7] L. Zhao, R. Mulkern, C.H. Tseng, D. Williamson, S. Patz, R. Kraft, R.L. Walsworth, F.A. Jolesz, M.S. Albert, Gradient-echo imaging considerations for hyperpolarized 129Xe MR, J. Magn. Reson. B 113 (1996) 179–183.

[8] J.M. Wild, M.N. Paley, M. Viallon, W.G. Schreiber, E.J. van Beek, P.D. Griffiths, k-space filtering in 2D gradient-echo breath-hold hyperpolarized 3He MRI: spatial resolution and signal-to-noise ratio considerations, Magn. Reson. Med. 47 (2002) 687–695.

[9] A. Oppelt, R. Graumann, H. Barfuss, H. Fischer, W. Hartl, W. Shajor, FISP – a new fast MRI sequence, Electromedica 54 (1986) 15–18.

[10] M.L. Gyngell, The application of steady-state free precession in rapid 2DFT NMR imaging: FAST and CE-FAST sequences, Magn. Reson. Imaging 6 (1988) 415–419.

[11] E. Durand, G. Guillot, L. Darrasse, G. Tastevin, P.J. Nacher, A. Vignaud, D. Vattolo, J. Bittoun, CPMG measurements and ultrafast imaging in human lungs with hyperpolarized helium-3 at low field (0.1 T), Magn. Reson. Med. 47 (2002) 75–81.

[12] J. Svensson, S. Mansson, E. Johansson, J.S. Petersson, L.E. Olsson, Hyperpolarized 13C MR angiography using TrueFISP, Magn. Reson. Med. 50 (2002) 256–262.

[13] J.P. Mugler III, M. Salerno, E.E. de Lange, J.R. Brookeman, Optimized TrueFISP hyperpolarized 3He MRI of the lung yields a 3-fold SNR increase compared to FLASH, Proc. Int. Soc. Man. Reson. Med. 10 (2002) 2019.

[14] J.M. Wild, L. Kasuboski, K. Teh, N. Woodhouse, S. Fichele, M.N.J. Paley, SSFP imaging with hyperpolarized 3He: experiments and simulations, Proc. Int. Soc. Man. Reson. Med. 13 (2005) 50.

[15] B.A. Hargreaves, S.S. Vasanawala, J.M. Pauly, D.G. Nishimura, Characterization and reduction of the transient response in steady-state MR imaging, Magn. Reson. Med. 46 (2001) 149–158.

[16] K. Scheffler, On the transient phase of balanced SSFP sequences, Magn. Reson. Med. 49 (2003) 781–783.

[17] K.D. Merboldt, W. Hänicke, M.L. Gyngell, J. Frahm, H. Bruhn, Rapid NMR imaging of molecular self-diffusion using a modified CE-FAST sequence, J. Magn. Reson. B 82 (1989) 115–121.

[18] D. Le Bihan, R. Turner, J.R. MacFall, Effects of intravoxel incoherent motions (IVIM) in steady-state free precession (SSFP) imaging: application to molecular diffusion imaging, Magn. Reson. Med. 10 (1989) 324–337.

[19] E.X. Wu, R.B. Buxton, Effect of diffusion on the steady-state magnetization with pulsed field gradients, J. Magn. Reson. B 90 (1990) 243–253.

[20] C.E. Carney, S.T. Wong, S. Patz, Analytical solution and verification of diffusion effect in SSFP, Magn. Reson. Med. 19 (1991) 240–246.

[21] A. Vignaud, E. Brief, X. Maitre, E. Durand, L. Darrasse, G. Guillot, J. Choukeife, P.J. Nacher, G. Tastevin, In vivo hyperpolarized helium-3 transverse relaxation at 1.5 T, in: Proceedings of ESMRMB, 2002, p. 417.

[22] J.P. Mugler III, M. Salerno, J.R. Brookeman, Reducing diffusion-induced signal loss in hyperpolarized 3He MRI, Proc. Int. Soc. Mag. Reson. Med. 10 (2002) 2018.

[23] J.M. Wild, S. Fichele, N. Woodhouse, M.N.J. Paley, P.D. Griffiths, A. Swift, E.J.R. van Beek, Assessment and compensation of macroscopic field inhomogeneity artifacts in gradient echo 3He MRI, in: Proceedings of Helion02, International Workshop on Polarized He-3 Beams and Gas Targets and Their Applications, Oppenheim, Germany, 2002.

[24] A. Oregioni, N. Parizel, P.L. de Sousa, D. Grucker, Fast measurement of relaxation times by steady-state free precession of 129Xe in carrier agents for hyperpolarized noble gases, Magn. Reson. Med. 49 (2003) 1028–1032.

[25] N. Bloembergen, R.V. Pound, Radiation damping in magnetic resonance experiments, Phys. Rev. 95 (1954) 8.

[26] G.P. Wong, C.H. Tseng, V.R. Pomeroy, R.W. Mair, D.P. Hinton, D. Hoffmann, R.E. Stoner, F.W. Hersman, D.G. Cory, R.L. Walsworth, A system for low field imaging of laser-polarized noble gas, J. Magn. Reson. 141 (1999) 217–227.

[27] K. Teh, N. de Zanche, J.M. Wild, Radiation damping effects in HP 3He at high field strengths, Proc. Int. Soc. Man. Reson. Med. 13 (2005) 218.

[28] S.B. Reeder, D.A. Herzka, E.R. McVeigh, Signal-to-noise ratio behavior of steady-state free precession, Magn. Reson. Med. 52 (2004) 123–130.

[29] J.P. Mugler III, J.F. Mata, H.T. Wang, W.A. Tobias, G.D. Cates, J.M. Christopher, J.L. Missel, A.G. Reish, K. Ruppert, J.R. Brookeman, K.D. Hagspiel, The apparent diffusion coefficient of Xe-129 in the lung: preliminary human results, Proc. Int. Soc. Man. Reson. Med. 11 (2004) 769.

[30] J.M. Wild, S. Fichele, N. Woodhouse, M.N.J. Paley, L. Kasuboski, E.J.R. van Beek, 3D volume-localized pO₂ measurement in the human lung with 3He MRI, Magn. Reson. Med. 53 (2005) 1055–1064.

[31] J.M. Wild, S. Fichele, N. Woodhouse, M.N.J. Paley, P.D. Griffiths, A. Swift, E.J.R. van Beek, Assessment and compensation of susceptibility artifacts in gradient echo MRI of hyperpolarised 3He gas, Magn. Reson. Med. 50 (2003) 417–422.

[32] J. Parra-Robles, A.R. Cross, G.E. Santyr, Theoretical signal-to-noise ratio and spatial resolution dependence on the magnetic field strength for hyperpolarized noble gas magnetic resonance imaging of human lungs, Med. Phys. 32 (2005) 221–229.

[33] M. Salerno, J.R. Brookeman, E.E. de Lange, J.P. Mugler 3rd., Hyperpolarized 3He lung imaging at 0.5 and 1.5 Tesla: a study of susceptibility-induced effects, Magn. Reson. Med. 53 (2005) 212–216.

[34] R.W. Mair, M.I. Hrovat, S. Patz, M.S. Rosen, I.C. Ruset, G.P. Topulos, L.L. Tsai, J.P. Butler, F.W. Hersman, R.L. Walsworth, 3He lung imaging in an open access, very-low-field human magnetic resonance imaging system, Magn. Reson. Med. 53 (2005) 745–749.